COMMUNICATION

Revealing perovskite formation kinetics during chemical vapour deposition

Received 00th January 20xx,
Accepted 00th January 20xx

DOI: 10.1039/x0xx00000x

Thierry A. Moser[a], Kerem Artuk[a], Yan Jiang*[a], Thomas Feurer[a], Evgeniia Gilshtein[a], Ayodhya N. Tiwari[a] and Fan Fu*[a]

Amongst a number of deposition methods for perovskite layers, vapour based ones are promising for large area industrial production of solar cells. Different variants of such methods and high efficiencies have been reported recently, but there remains a lack of understanding on the formation process of perovskite layers with 2-step vapour deposition. Here, we present a new reactor design for controlled investigation of the reaction kinetics for conversion of evaporated metal halide precursor layer (such as a mixture of lead iodide and cesium bromide) into perovskite layer by exposure to an organo-halide (such as formamidinium iodide) vapour under stable isobaric-isothermal conditions. With this new concept of gas flow reversal in tubular reactor, we overcome an inherent problem of the lack of control over the precise start and end of the conversion process. We investigated the formation reaction of mixed cation $(Cs_{0.04}FA_{0.96})PbI_3$ perovskite in well-defined intermediate states to elucidate the influence of processing conditions on the kinetics of perovskite and other phase formations. High conversion rate of up to 60 nm/min is achieved with a well-controlled abrupt start and end of the vapor supply. Using our deposition method, a semitransparent solar cell with a power conversion efficiency (maximum power tracking) of 9.6% on a designated area of 0.27 cm^2 is achieved in the initial phase of development where the charge extracting layers and interfaces are yet to be optimised.

Introduction

The past decade has witnessed the unprecedented advances in power conversion efficiency (PCE) of thin film solar cells based on metal halide perovskites (ABX_3, A = Cs, methylammonium (MA), formamidinium (FA); B = Pb, Sn; X = Cl, Br, I [1,2]), with a certified efficiency at 25.2% on ~ 0.1 cm^2. [3,4] An industrially promising approach for the deposition of perovskite thin films is the chemical vapour deposition (CVD)[5,6]. Although in literature various technical implementations and also naming (e.g. H-CVD: hybrid chemical vapour deposition[7], VASP: vapour assisted solution processing[8], ITCVD: in-situ tubular chemical vapour deposition[9], LP-CVD: Low pressure CVD[10]) of this method can be found, the underlying principle is the same: An organo-halide material (e.g. FAI) is sublimed and its vapour is transported to the substrate, where it reacts with a pre-deposited metal halide precursor layer (e.g. a $CsBr/PbI_2$).

While this precursor layers can be deposited from solution[11,12], they can also be thermally evaporated, which maintains the advantage of high-uniformity and scalability. Tong et al. converted a sequentially evaporated $CsBr/PbI_2$ stack with FAI for 100 minutes at 140°C to realize a compositionally graded absorber and achieved an opaque device with a PCE of 18.2% (0.09 cm^2) [13]. Qiu et al. also employed an all-vapour approach by converting a co-evaporated $CsBr/PbI_2$ precursor with FAI vapour. They realized an opaque mini-module with a designated area of 91.8 cm^2 and 9.34% PCE. This corresponds to a loss of only 1.3%/decade of scaled area when comparing to their champion efficiency of 13.3% on 0.09 cm^2.[14]

Despite the advances in power conversion efficiency, perovskite formation kinetics during the CVD process has remained elusive. The CVD process is usually carried out in a reaction chamber that can be heated and evacuated to provide suitable sublimation and reaction conditions. Under such conditions, both the sublimation and the transport of the organic species already starts and accelerates during the heat-up period and also doesn't immediately stop during the cool-down period. This means that the conversion reaction is not happening under constant conditions but continuous changes in temperature and vapour pressure of the organic species are occurring. But in order to study the perovskite formation kinetics during the CVD process, stable conditions and a well-defined reaction time window are required.

[a] Laboratory for Thin Films and Photovoltaics, Empa – Swiss Federal Laboratories for Materials Science and Technology, Ueberlandstrasse 129, Duebendorf 8600, Switzerland. *E-mail:* fan.fu@empa.ch; yan.jiang@empa.ch

Electronic Supplementary Information (ESI) available: [details of any supplementary information available should be included here]. See DOI: 10.1039/x0xx00000x

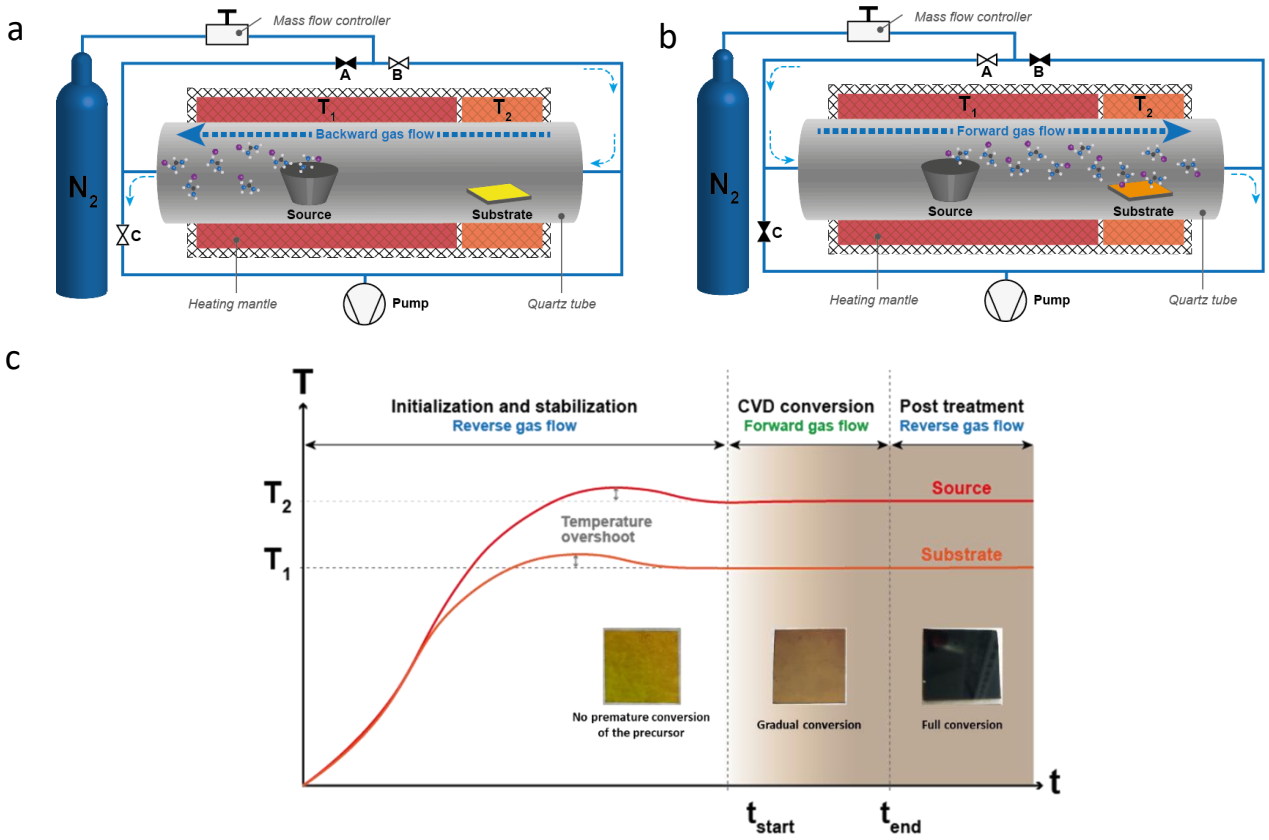

Figure 1: Controlled isothermal-isobaric CVD process. a) and b) Schematic of the CVD reactor, allowing quick reversal of carrier gas flow. Depending on the flow direction, the premature reaction process is prevented before attaining the stabilized thermal conditions. c) Time-temperature-dependent reaction graph with control of carrier gas flow direction: Reverse gas flow allows to stabilize the temperature zones without occurrence of premature conversion reaction. Changing the gas flow direction allows to start and stop the conversion reaction. Additionally, the sample can be kept in the reactor for a post conversion annealing treatment if needed.

In this work, we present the deposition of a mixed cation $(Cs_{0.04}FA_{0.96})PbI_3$ perovskite via a hybrid chemical vapour deposition process where we are able to achieve the required control by decoupling the heating and reaction step. Through the systematic study of the perovskite film formation kinetics, we find that the perovskite formation reaction is either mass transport or diffusion-limited, depending on the temperature of the FAI sublimation zone. Furthermore we find that the conversion reaction kinetics are not only controlled by the FAI sublimation temperature but also the substrate temperature. Understanding the kinetics allows us to deposit high-quality perovskite film with a growth rate of up to 60 nm/min. Additionally, we observe the formation of additional phases besides the desired perovskite under certain processing conditions. These side reactions have to be avoided and therefore are important to consider for the CVD deposition of phase pure perovskite absorbers. As proof-of-concept, the CVD process was used to fabricate a semi-transparent PSC without any post-treatment of the absorber or optimization of the contact layer. The final device exhibits a power conversion efficiency of 10.6%.

Results and discussion

Isothermal-isobaric CVD process

In the works published so far on the subject of perovskite absorbers deposited via CVD we encounter systems where the organic vapour is allowed to come into contact during the complete process. This means that the conversion already starts (resp. continues) during the heat-up (resp. cool-down) of the system. Therefore the conversion is not occurring under constant conditions (i.e. substrate/source temperature, pressure, concentration of the organic vapour).

To achieve better control over the CVD process we modified the classical concept of a tubular reactor. Our set-up allows for the selective injection of the carrier gas from either side of the reaction chamber. Thus, a gas flow in both directions is possible – an approach that has yet not been employed in perovskite research. With our set-up, we can at first have a carrier gas flow in the reverse direction (i.e., going from the substrate side towards the source side), as depicted in **Figure 1a**. Under this condition, we ramp the two heating zones to their distinct target temperatures with the carrier gas preventing premature contact between the organic vapour and the precursor. Once pressure and temperatures stabilized, the flow direction of the carrier gas is reversed, enabling the vapour and precursor layer to get into contact (see **Figure 1b**). Reversing the flow direction a second time allows stopping the conversion reaction.

Table 1: Conditions studied for their effects on reaction kinetics and phase evolution.

Condition	Substrate temp. T_2 [°C]	Source temp. T_1 [°C]
A	160	190
B	180	190
C	160	210
D	180	210

In short, our CVD setup allows the conversion reaction to happen in isothermal and isobaric conditions for a well-defined time window. While this is not expected to directly improve the quality of the final perovskite layer, this unlocks the possibility to conduct time-resolved mechanism studies on the effect of temperature and pressure conditions during the CVD process. For our study we employed a co-evaporated $CsBr/PbI_2$ layer with an atomic percentage of 4% CsBr as confirmed by X-ray photoelectron spectroscopy (XPS; **Figure S1**) and convert it with our CVD set-up with FAI vapour. This composition was chosen as cesium and formamidinium based perovskites have shown high stability and power conversion efficiencies. [15–17] Albeit the precursor contains bromine, XPS did not show its presence in the final perovskite (**Figure S2-S3**) as it is replaced by iodine by ion exchange during the CVD process.

Kinetics of the conversion reaction

To investigate the reaction kinetics of the CVD process, we estimated the conversion fraction Γ(t) of the precursor layer after different reaction times t as this gives a measure for the progress of the reaction. Following the approach of Ummadisingu et al.[18] the conversion fraction was defined as

$$\Gamma(t) = \frac{A(t)}{A_{fc}} * 100\%$$

where A(t) is the absorbance of the mixed perovskite layer after reaction time t and A_{fc} is the absorbance of a fully converted layer (~500 nm). This conversion fraction was calculated from UV-Vis spectroscopy data using the Lambert-Beer relationship[19]. Details on the optical model applied, the underlying calculations are given in the supplementary information (**Figure S4-S6**).

Figure 2 shows the conversion fraction as a function of reaction time for four different temperature conditions, specified in Error! Reference source not found.. For all the runs precursor thickness and composition as well as pressure and mass flow of the carrier gas were kept the same.

The fastest kinetics is observed for condition C (160-210), where a full, homogeneous conversion of a 250 nm $CsBr/PbI_2$ precursor layer is achieved in only 8 minutes.

In literature, the required time of the CVD conversion process is often between one and three hours [9,12,20]. This is due to the slow thermal response of conventional tube furnaces and the low heating rates that need to be employed to avoid thermal overshoots. Hoerantner et al. on the other hand, reported a high-speed vapour deposition technique that only requires a three-minute-long step for the conversion of a 200 nm thick PbI_2 precursor layer into $MAPbI_3$ perovskite[21]. This already demonstrated that the actual conversion reaction can be achieved at shorter times. In an industrial in-line system, where the substrate would be continuously fed into the reactor and an initialization step is not needed, the actual required conversion time is the key parameter that determines the maximally achievable throughput. For the design of the CVD equipment such knowledge of the reaction kinetics is essential.

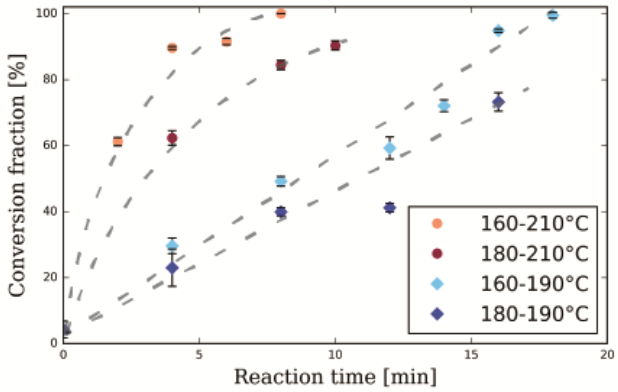

Figure 2: Reaction kinetics of perovskite formation at different conditions shown by the change of the conversion fraction under different conditions with time. The dashed lines serve as guide for the eye.

One can see that a higher source temperature T_1 strongly increases the conversion rate. This shows that the speed of conversion can be controlled by the sublimation rate of the FAI. Possibly, the rate of conversion could be even further accelerated by increasing the source temperature. But such high kinetics might impede the controllability and reproducibility of the process unless sophisticated temperature and gas flow controls are used.

Comparing the slow and fast (i.e., low resp. high source temperature T_1) conversion regime, we observe two different behaviour. When working with a low source temperature (i.e., condition A (160-190) and B (180-190)), the conversion rate is constant and not affected by the increasing thickness of the perovskite layer. In the case of high source temperature (i.e., condition C (160-210) and D (180-210)) we observe a decrease in the conversion rate with time. This indicates that at a low source temperature, the reaction kinetics are governed by the mass-transport of the FAI vapour. The decrease in conversion rate at a high substrate temperature implies that the solid-state diffusion becomes the dominant factor.

While the influence of the source zone temperature T_1 on the reaction kinetics was anticipated, the influence of the substrate zone temperature T_2 shows the reverse effect: For both slow and fast conversion regime, the reaction speed was lowered when a higher substrate zone temperature T_2 was chosen. A higher substrate temperature T_2 usually is expected to provide more thermodynamic driving force for the reaction between the reactants and also facilitate the interdiffusion, so one could expect to observe an acceleration of the reaction. Nevertheless, it is important to bear in mind that the substrate temperature both affects the condensation dynamics of the FAI vapour and

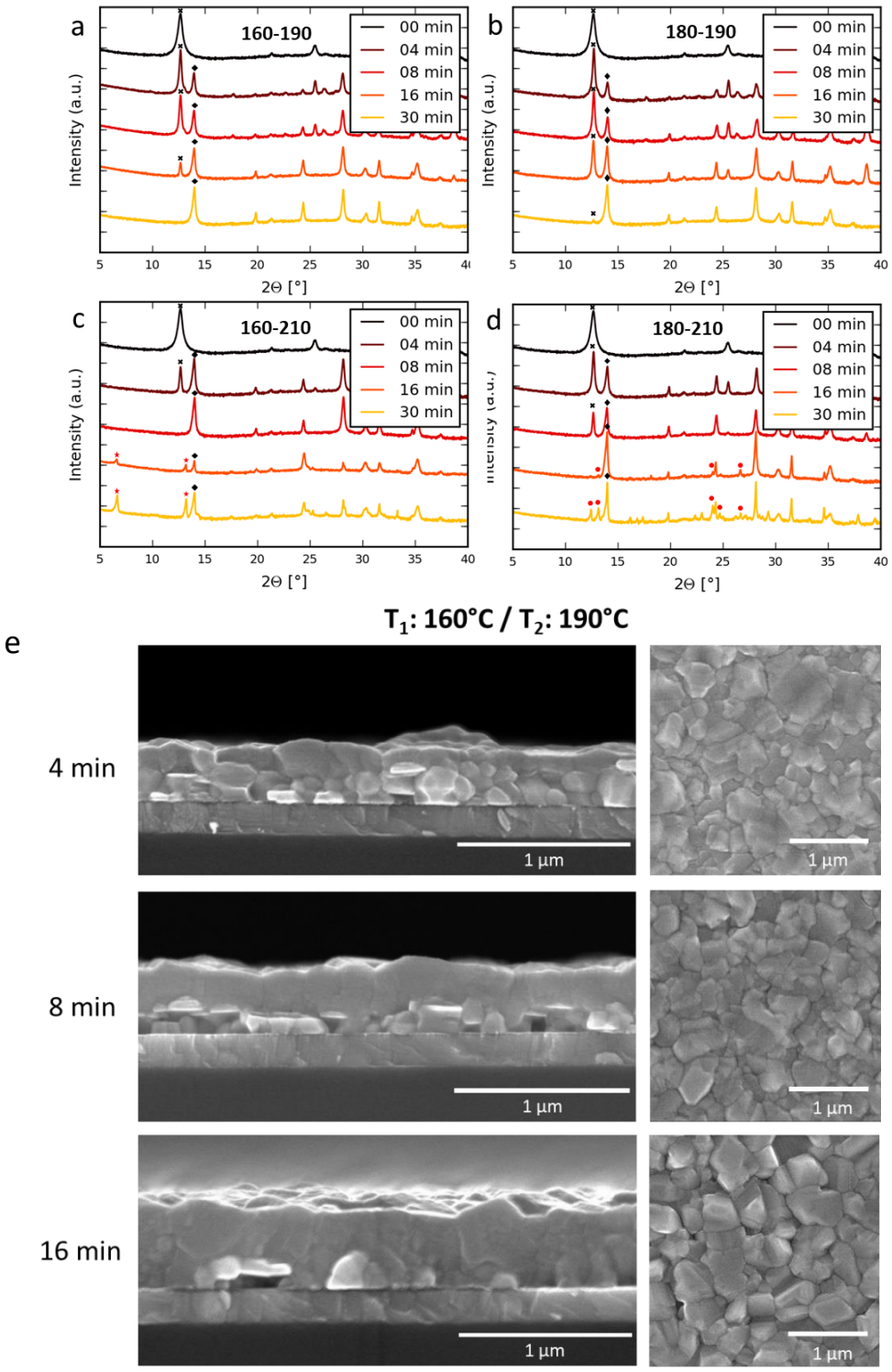

Figure 3: Phase evolution during CVD conversion of perovskite for different conditions of reaction time and temperatures (in °C) of substrate and evaporation source. a) 160-190, b) 180-190, c)160-210, d) 180-210. During the perovskite formation, the precursor peak (indicated by **x**) at 12.7° is continuously fading and the perovskite phase peak (indicated by ♦) gains intensity. In c) and d) the formation of additional 'overconversion' phases (indicated by ● and★) is observed once the precursor is converted completely. e) SEM crosssection and top-views of layers after 4 min, 8 min and 16 min reaction time with the temperature zone at 160°C and the source zone at 190°C

the decomposition reaction of the perovskite. A lower temperature T_2 will result in higher rate of condensation on the substrate surface (i.e., a higher supply of FAI to the conversion reaction) and a slower decomposition reaction. These two effects lead to the accelerated kinetics of the conversion reaction at a lower temperature T_2.

Phase evolution of conversion reaction

To probe the phase evolution during the CVD process, we performed X-ray diffraction measurements on the thin films converted at the four different conditions for various times. These phase evolutions are depicted in **Figure 3**. The two main peaks at 12.7° and 14.0° correspond to the PbI_2 (110) and the (110) perovskite crystalline planes, respectively. They reflect the conversion process under different conditions: For the fast conversion regime (i.e., T_1 = 210°C) the peak of the precursor phase vanishes and the perovskite peak rises very quickly with time while these effects are more gradual for the slow conversion regime (i.e., T_1 = 190°C). Again, we observe that a higher substrate temperature T_2 causes a slower change of the peak intensities.

Under conditions C (160-210) and D (180-210) additional phases are evolving after the precursor has transformed into perovskite. Under condition C (160-210), two new peaks start to show up at 6.6° and 13.2° for a conversion time of 16 minutes and more. Under condition D (180-210) new peaks are present at 12.5, 24.0°, 24.7° and 26.7° when the CVD process is run for 16 minutes or more. Formation of these new phases is accompanied by strong changes in optical properties. Initially the transparent yellow precursor layers turn to a dark brown/black appearance indicating the conversion to perovskite. Subsequently the appearance would change again depending on the conditions of the process. Under condition C (160-210) the layers turned to an inhomogeneous yellow-orange hue, while for condition D (180-210) the layers showed a grey, milky colour and macroscopic cracks. The different appearances can be seen in **Figure 5f**. We would like to point out that the apparent inhomogeneity of the precursor layer and the layers converted at 170-180°C, 160-190°C and 220-200°C in those photographs stems from the background paper substrate and is not due to the layers themselves.

A possible explanation for the emergence of these additional peaks could be the condensation and crystallization of pure source material (i.e., formamidinium iodide) on the sample. The XRD pattern taken from pure formamidinium iodide powder is displayed in **Figure S7** and no overlap of the diffraction peaks with the ones observed in our CVD samples could be found. We therefore assume that these additional phases stem from the reaction between the already formed perovskite phase and the formamidinium vapour. This conclusion is in line with work conducted by Leyden et al. where during CVD-deposition of $FAPbI_3$ foreign phases together with variations of the optical appearance were observed, which they attributed to a FAI-rich phase[20]. We term such layers with additional phases as 'over-converted'. To study the morphological evolution of the perovskite formation, we examined the different stages with secondary-electron microscopy (SEM). **Figure 3e** shows the top-view and cross-sectional SEM micrographs of the layers processed under condition A (160-190) for 4, 8 and 16 minutes. The series of cross sections shows that the perovskite phase forms a continuous layer over the thinning precursor layer and continues growing until only single grains of precursor are left at the perovskite-substrate interface. In general, the conversion

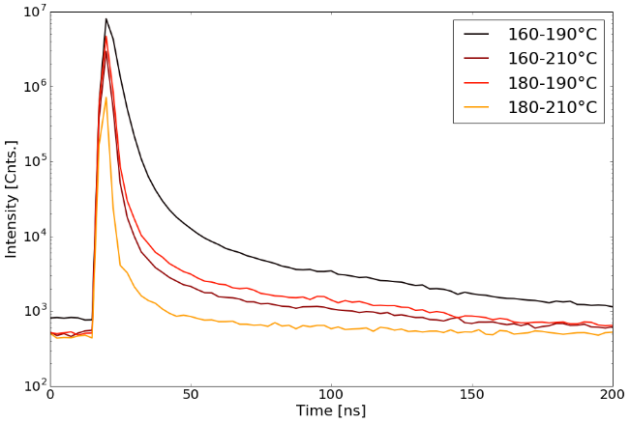

Figure 4: TRPL measurements of perovskite films on fused silica grown under different CVD conditions.

occurs uniformly and creates a flat and pin-hole free perovskite layer. We assessed the grain size distribution for the four different conditions from top-view SEM micrographs (see **Figure S11**), which show that that a faster conversion reaction favours the formation of smaller grains. This observation can be explained by the common theory of crystallization: A faster conversion reaction is expected to create a larger number of nucleation sites where the perovskite crystals can grow, thus creating many small crystallites. Additionally, the reaction time determines the Ostwald ripening. For a slow conversion, the opposite effects, i.e. a lower number of nucleation sites and a higher degree of Ostwald ripening, are expected. The final grains of the perovskite show diameters of a few hundred nanometers. The corresponding micrographs are shown in **Figure S9-S11**. ~~As no differences could be found, we conclude that the final morphology is likely to be mainly determined by other parameters (such as the morphology of the metal halide precursor and the pressure during CVD) than the temperature respectively the growth rate.~~

Time-resolved photoluminescence results

Figure 4shows the result of time-resolved photoluminescence (TRPL) measurements conducted on perovskite layers grown on fused silica under the four different conditions A-D. A higher luminescence intensity and a longer carrier lifetime was observed for a slow conversion and a low substrate temperature during the conversion.

The TRPL decay shows a very fast quenching of the photoluminescence. This indicates that the recombination of the charge carriers is strongly dominated by non-radiative recombination. From a bi-exponential fitting we estimated a radiative lifetime of 55 ns for CVD condition A (160-190°C). For the conditions B, C and D no acceptable fitting was possible. Such low lifetimes are quite typical and are still one of the major challenges for vacuum-deposited absorbers[12,21–23]. Perovskite bulk is commonly assumed to be highly defect tolerant and mainly the surface defects are thought to be responsible for non-radiative recombination of charge charriers[24,25]. We assume that our vapour phase deposition of perovskite favours

the formation of surface defects, which explains the low carrier lifetimes of the pristine absorbers.

Isochronal process map

To gain further insight into the CVD process and the formation of the 'overconverted' phases, we processed perovskite films at a fixed conversion time of 30 minutes and source temperatures T_1 ranging from 180° to 220°C and substrate temperatures T_2 ranging from 150° to 220°C. The results of the XRD measurements of the fabricated samples are visualized in **Figure 5**. The intensity maps in **Figure 5a** and **b** show the (110) perovskite phase reflection at 14° and the (110) PbI_2 precursor phase reflection at 12.6°, respectively. Additionally, the reflections at 6.6° and at 24° which stem from the 'over-converted' phase were mapped in **Figure 5c** and **d**.

One can see that the perovskite phase is present after processing at nearly each condition except for the extreme case of a substrate temperature of 220°C. Meanwhile the precursor is only present for the case of the lowest source temperature (i.e., T_2 = 180°C) or a substrate temperature T_2 equal or above 200°C. For the two 'over-converted' phases, we find two different regimes where they start to appear. On the one hand, the peak at 6.6° is observed for low substrate temperatures (i.e., T_2< 170°C) together with elevated source temperatures (i.e., T_1 > 190°C). On the other hand the peak at 24.0° is observed for medium substrate temperature (i.e., 170°C < T_2 < 210°C) in combination with high source temperatures (i.e., T_1 > 200 °C).

Based on the XRD maps in **Figure 5a-d**, we constructed an isochronal processing map shown in Figure 1**Figure 5e**. The map visualizes the outcome of the CVD process of 30 minutes, depending on the set temperature of the source zone and the substrate zone.

For a source temperature T_1 below 190°C we define an area of 'insufficient FAI sublimation'. In this region, the sublimation rate of the source material (i.e., formamidinium iodide) is very low. In consequence, the sample is only weakly converted, even after the 30 minutes of processing time. Clearly, this sets a lower boundary for a useful processing window in which the desired perovskite absorber can be fabricated. Another boundary is imposed by the thermal stability of the perovskite. For substrate zone temperatures above 200°C there is no perovskite but only precursor present after the CVD process. This region is named 'decomposition' as the perovskite - if formed at all – would not withstand the combination of reduced pressure and elevated temperature and decompose.

The intriguing aspect of this processing map are the two different 'overconversion regions' in which additional - unwanted - phases are formed. This does not only impose additional boundaries to the processing window but it proves that the perovskite phase is not the only product that can be formed from cesium bromide, lead iodide and formamidinium iodide.

It is important to note that the 'overconverted' phases are formed *via* the perovskite phase, after extended reaction times and at high FAI vapour concentrations. This means that also thicker precursor layers can be converted without the formation of the overconverted phase if the appropriate CVD conditions are chosen. We also do not observe a single-phase layer but rather a blend between perovskite and 'overconverted' phase. These observations indicate that we are either dealing with a thermodynamic equilibrium or that the formation of the 'overconverted' phases is kinetically hindered. We see that at the same source temperature (e.g. 200°C) the formation of the 'overconverted' phase can be prevented by using a higher substrate zone temperature. This supports the assumption of a thermodynamic equilibrium. The higher substrate temperature decreases the condensation of the FAI vapour, which reduces its chemical potential in the reaction. If there were a kinetic hindrance, we would expect that the 'overconverted' phase is formed faster at a higher temperature. It is essential to understand under which conditions this 'overconversion' reaction occurs for the sake of achieving high quality perovskite absorbers. We have already observed that the 'overconversion' strongly changes the optical properties of the fabricated layer. Clearly this deteriorates the performance of the layer when used as an absorber in a photovoltaic device. In the work of Leyden et al. they observed similar 'overconversion' behaviour during the CVD deposition of $FAPbI_3$ but did not further investigate under which CVD conditions it occurred[20]. They also showed that the phase formation was reversible, which supports the notion of a thermodynamic equilibrium. Still the final device performance was impaired by the reversal, indicating that it is better to completely avoid the overconversion reaction.

Scalability

To demonstrate the scalability of the CVD process, we converted a precursor layer deposited on a 5x5 cm^2 fused silica substrate and measured the UV-Vis response and XRD patterns in 9 different areas. The XRD shows a single phase perovskite layer in all probed areas without any precursor or overconversion phase present. From the UV-Vis results we see that the perovskite layer is thickest in the middle of the substrate and up to 10% thinner in the edge/corner regions. This non-uniformity is not stemming from the CVD conversion but rather from the PVD deposition of the precursor. Profilometry measurements show that the precursor template also exhibits a ~10% lower thickness in the edge/corner regions. These results suggest that we can uniformly convert precursor layers on larger substrates. Still it is important to mention, that although a high source temperature (i.e. T1 =210°C, high FAI vapour concentration) was used, the reaction time had to be extended to 20 minutes to achieve full conversion. This shows that our experimental CVD set-up is susceptible to the precursor area present. Nevertheless, we are convinced that the high growth rate achieved on small substrates would be feasible with CVD in a uniform manner with appropriate reactor design. The corresponding graphs can be found in **Figure S12**.

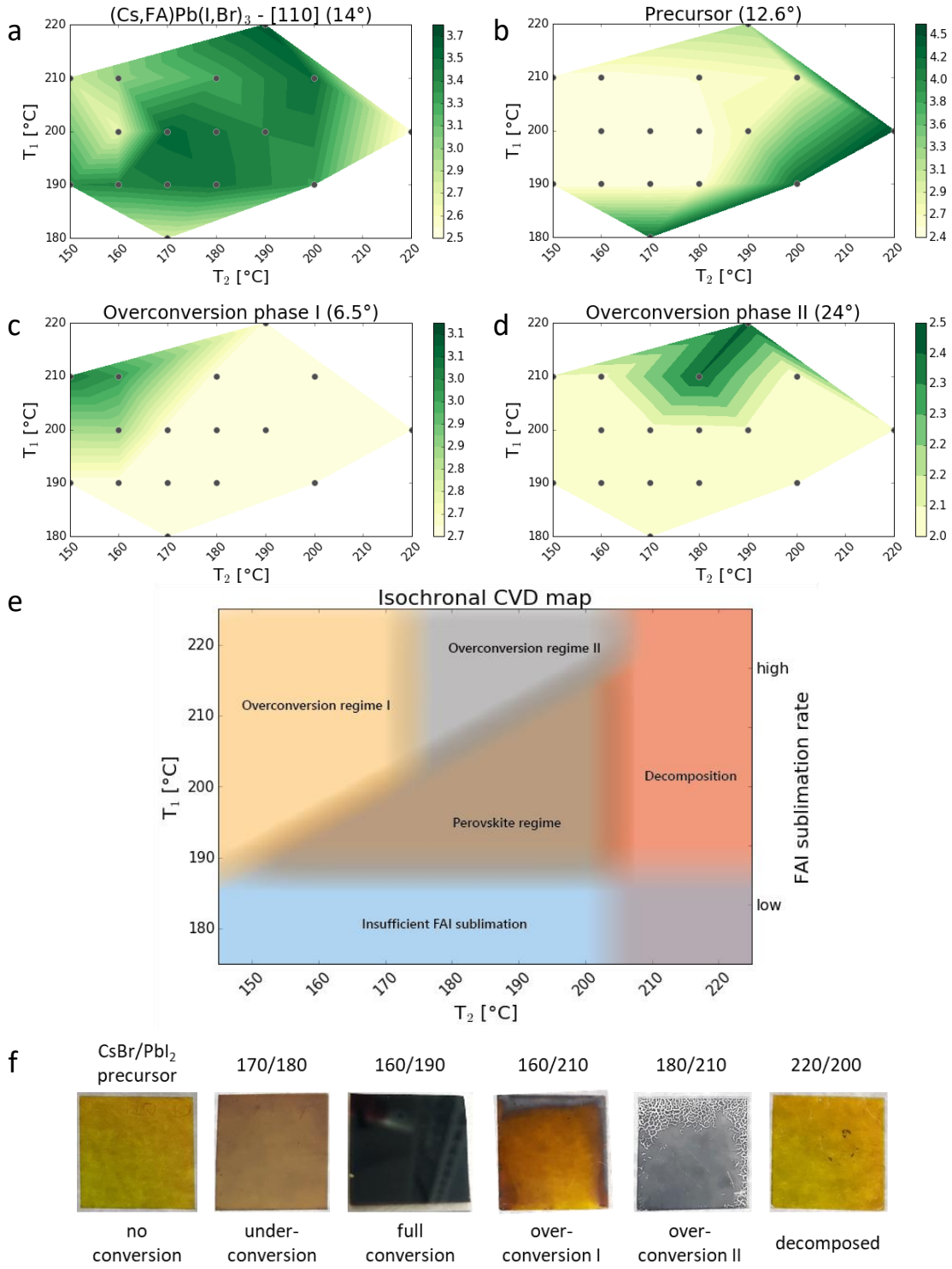

Figure 5: a-d) Intensity maps of selected XRD peaks after 30 minutes CVD processing time. The black dots represent the individual data points. All samples were fabricated and measured under identical conditions, varying only the temperature of the source and substrate zone in the CVD reactor. a) Perovskite (110), b) PbI_2(110), c) overconverted phase I and d) overconverted phase II intensity map. e) Schematic isochronal CVD processing map showing five different regimes. f) Representative images of samples processed in the different regions. The apparent inhomogeneity of the sample stems from the underlying paper substrate used during photography.

Device fabrication

Using the novel CVD method, we fabricated a semi-transparent perovskite solar cell with an architecture of ITO/PTAA/Perovskite/PCBM/ZnO(np)/AZO/Ni-Al-grid (ITO: Indium tin oxide, PTAA: Poly(triaryl amine), PCBM: Phenyl-C61-butyric acid methyl ester, ZnO(np): Zinc oxide nanoparticles, AZO: Aluminium-doped zinc oxide)-.

In the range of 800-1200 nm an average transmittance of 56.1% was measured (see **Figure S13**). The low transmittance in the near infrared region can be explained by the lack of an anti-

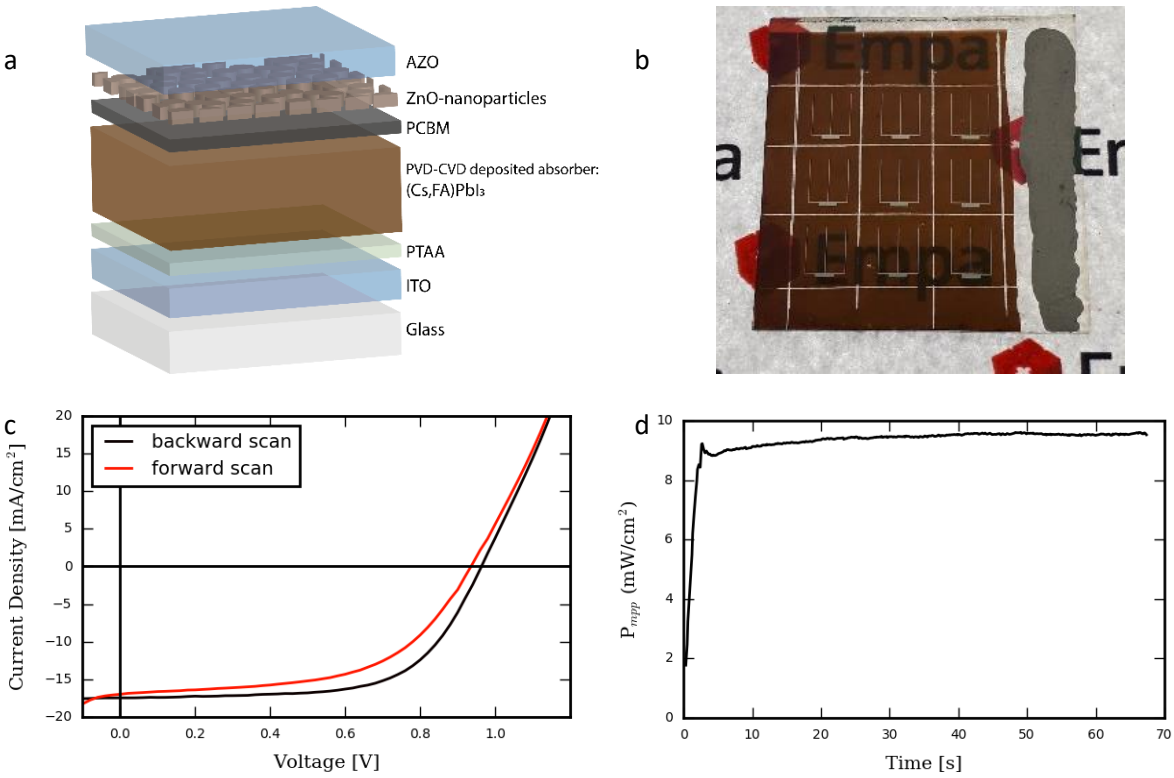

Figure 6: Semitransparent device based on a two-step sequential vapour-deposited perovskite absorber. a) Schematic architecture, b) photograph of the final device, c) J-V characteristics of forward and backward scan and d) MPP measurement of the champion device

reflection coating and the high free carrier absorption of the ITO substrate present (see **Figure S14**). This issue could be alleviated by the use of high-mobility hydrogenated indium oxide, which shows excellent NIR transmittance[26,27].

The cell area of 0.27 cm² was defined by mechanical scribing. A schematic of the architecture and a photograph of the devices are shown in **Figure 6a** and **b** , respectively. For the conversion of the precursor, the condition A (160-190) and a conversion time of 20 minutes was chosen in order to reach a degree of conversion close to 100%. The measured JV characteristics in forward and backward direction and the maximum power point (MPP) measurement are shown in **Figure 6 c** and **d**, respectively. For our champion device a power conversion efficiency of 10.6% was measured when scanning in backward direction. ~~To the best of our knowledge, this is the highest reported value for the semi-transparent perovskite solar cell fabricated by the sequential two-step vapour deposition method.~~ The stabilized efficiency measured with maximum power point (MPP) tracking is 9.6%. We attribute this lower performance to the significant hysteresis revealed by the forward scan (**Figure 6a**). The statistics of the J-V parameters obtained from the backward scans of all 9 devices on the substrate are shown in **Figure S15**. As the device stack has not been optimized we expect that the device performance can be considerably increased.

Conclusions

We developed an isobaric-isothermal CVD process that allowed us to study the reaction kinetics and the phase evolution during the deposition of mixed $(Cs_{0.04}FA_{0.96})PbI_3$ perovskite. Our study shows how the temperature of source and substrate affect the conversion reaction kinetics. We demonstrated the uniform conversion on 5x5 cm substrates and achieved perovskite films with a growth rate of 60 nm/min, which is an important parameter from an industrial manufacturing point of view. We also show that undesired side reactions can occur during the CVD conversion that result in the formation of unfavourable phases. This imposes additional boundaries to the process as to achieve high quality perovskite layers, these reactions need to be avoided by controlling process parameters.

Using our new sequential vapour deposition method we fabricated semi-transparent PSCs with a champion PCE of 9.6% on a designated area of 0.27cm².

Materials & Method

Perovskite layer growth

All chemicals were used as received, without any further purification or treatment.

To exclude substrate effects, the perovskite layers were always grown on the same substrate, namely PTAA coated ITO. The ITO substrates (R_s < 10 Ω / □ ,Zhuhai Kaivo Optoelectronics Co.) were washed by hand first, followed by ultra-sonication at 85°C in soap water, acetic acid solution, de-salted water and finally de-ionized water for 15 minutes each in the order given here. The ITO substrates were then dried with compressed nitrogen.

A PTAA layer was prepared by spin-coating a solution of 5 mg PTAA (Ossila) in 1 ml of Toluene. 50 µl of the solution was dropped onto the 2.5x2.5 cm² ITO substrate spinning at 6000

rpm and the rotation was continued for another 30 seconds. The layer was dried on a hot plate at 80°C for 5 minutes.

The ITO/PTAA substrate was then transferred to a thermal evaporation system where PbI_2 (99.999%, Sigma Aldrich) and CsBr (99.999%, Sigma Aldrich) were co-evaporated at an evaporation pressure of 3-6*10e-08 mbar to form the metal halide precursor layer. The deposition rate of lead iodide and cesium bromide were kept constant at 1.7 Å s^{-1} and 0.07 Å s^{-1}, respectively. The targeted deposition thickness of the lead iodide was set to 250 nm, which corresponds to a thickness of 10 nm of the cesium bromide.

The precursor layers were then transferred to the tubular CVD reactor.

For the CVD conversion, 0.2 g of formamidinium iodide (FAI, >99%, Greatcell Solar Materials) were loaded into a graphite crucible (Umicore). It was taken care that the FAI powder was evenly spread on the bottom of the crucible to achieve a constant free surface for sublimation during each run. The crucible and the precursor coated substrate were placed at the same position in their individual heating zone for each run. After loading, the system was pumped down until a pressure of <1 mbar was reached. Then nitrogen (99.999%, PanGas) carrier gas was injected via a mass flow controller such that a reverse flow was established (i.e., valve A closed, valve B and C open, see **Figure 1a**). The volume flow rate was set to 0.5 mbar*l/s (correspoding to approximately 30 sscm) which resulted in an equilibrium pressure of 7-8 mbar in the system during the following process step. With the carrier gas flowing, both substrate and source heating zones were heated up to their target temperatures ($T_{substrate}$: 150-220°C, T_{source}: 180-220°C) with high heating rate at the beginning and low heating rate when getting close to the target temperature to avoid overshooting. Once the target temperature were reached, the reverse flow was maintained for 10 minutes to establish thermal equilibrium. After equilibration, the conversion reaction was started by inverting the flow direction of the carrier gas to establish downstream flow (i.e., valve A was openend and subsequently valves B and C were closed). After the desired reaction time had passed, the conversion was halted by once again inverting the carrier gas flow and re-establishing the reverse flow. The system was kept under reverse flow for two minutes before the reactor was vented with nitrogen, opened and the sample was transferred to a glove box to cool down and keep exposure to humid air as low as possible.

Solar cell fabrication

The solar cell was fabricated with a layer structure of ITO/PTAA/Perovskite/PCBM/ZnO-nanoparticles/AZO/Ni-Al-grid. The initial ITO/PTAA/Perovskite layer stack was deposited as described above. For the CVD conversion of the metal halide precursor, the substrate zone was set to 160°C and the source zone was set to 190°C and the conversion reaction was allowed to take place for 20 minutes. The electron-transporting layer was deposited on top of the perovskite by spin-coating a 20 mg/ml solution of PCBM (PC61BM, 99.5%, SolenneBV). 50 µl of the solution were dropped at a substrate spinning speed of 4000 rpm and rotation was continued for 30 seconds. The layer was dried for 5 minutes at 80°C. A buffer layer of ZnO nanoparticles was then deposited by spin-coating. 50 µl of a dispersion of 2.5w% ZnO nanoparticles (particle size: 12 nm, Avantama) in isopropanol was dropped at a substrate spinning speed of 5000rpm and rotation was continued for 30 seconds. The layer was dried for 2 minutes at 80°C. Both spin-coating and drying steps were carried out in a nitrogen filled glove box. A layer of aluminium doped zinc oxide (AZO) was deposited by RF-sputtering as top contact. Subsequently 50 nm of nickel followed by 4 µm of aluminium were e-beam evaporated through a shadow mask to form the contacting grids. The device was finalized by defining the designated area of 0.27 cm^2 by mechanical scribing down to the ITO back contact.

Characterization

XRD: X-Ray diffraction patterns were measured on an X'Pert Pro in Bragg-Brentano geometry using Cu-Kα1 radiation (λ = 1.5406 Å), scanning from 5 to 80° (2θ) with a step interval of 0.0167°. For the intensity maps the contours were extrapolated from triangulation between the individual data points.

UV-Vis: Reflectance and transmittance measurements were performed using a Shimadzu UV-Vis 3600 spectrophotometer equipped with an integrating sphere. The reflectance data was corrected for the instrumental response stemming from diffuse and specular reflections both on the sample as well as the reflectance measurements were carried out in a wavelength range from 300 to 1500 nm.

SEM: The SEM micrographs were taken with a Hitachi S-4800 Scanning Electron Microscope and a FEI NanoSEM 230 using 5-10 kV acceleration voltage. A thin layer (≈1 nm) of Pt was coated on top of the samples to avoid charging effects.

Solar cell characterization: The current density–voltage characteristics of the perovskite solar cell was measured in 4-terminal sensing with a Keithley 2400 source meter. The illumination was provided with a ABA class solar simulator and was calibrated to 1000 W m^{-2} using a certified single crystalline silicon solar cell. The sample stage temperature was kept at 22 °C during the measurements. The J–V measurements were performed in both forward (form −0.1 to 1.5 V) and backward (from 1.5 to −0.1 V) direction. The external quantum efficiency of the cells was measured with a lock-in amplifier. The probing beam was generated by a chopped white source (900 W, halogen lamp, 260 Hz) and a dual grating monochromator. The beam size was adjusted to ensure that the illumination area was fully inside the cell area. The shading effect of metallic grid was taken into account by including middle grid line into the illuminated area. A certified single crystalline silicon solar cell was used as the reference cell. White light bias of approximately 0.1 suns was applied during the measurement with a halogen bias lamp.

TRPL: Time-resolved photoluminescence was measured using the MicroTime 100 system from PicoQuant. A 639 nm pulsed laser diode (pulse width ~100 ps) was used. The excitation density was $2 \cdot 10^{12}$ photons·cm^{-2}pulse^{-1} (~ 3.1 J·s^{-1}·cm^{-2}). The

spot size was measured by a NanoScan2 beam profiler resulting in ~130 µm diameter. Acquisition times were 60 seconds and the pulse frequency 3 MHz. For the fitting procedure a bi-exponential decay was used and the first 35 ns after the signal peak were neglected.

XPS: X-ray photoelectron spectroscopy was performed using a Quantum2000 system from Physical Electronics with a monochromatic Al K_α source (1486.6 eV) and a base pressure below $8 \cdot 10^{-9}$ mbar. Survey spectra were recorded with an energy step size of 0.4 eV and a pass energy of 93.90 eV. Composition of the samples was analyzed using the MultiPak software.

Acknowlegdements

Financial funding from the Innovation and Networks Executive Agency of the European Commission (INEA, Project PERCISTAND, grant No. 850937), the Swiss Federal Office of Energy (SFOE, Project CIGSPSC, grant No. SI/501805-01) and the Swiss National Science Foundation (SNF, Project Bridge Power, grant No. 176552) is gratefully acknowledged.

We thank R. Carron and M. Ochoa Gomez for the helpful discussions and suggestions regarding the building of the optical model respectively regarding the photoluminescence measurements.

Conflicts of interest

There are no conflicts to declare.

Notes and references

1 S. F. Hoefler, G. Trimmel and T. Rath, *Monatshefte Für Chem. Chem. Mon.*, 2017, **148**, 795–826.

2 M. L. Petrus, J. Schlipf, C. Li, T. P. Gujar, N. Giesbrecht, P. Müller-Buschbaum, M. Thelakkat, T. Bein, S. Hüttner and P. Docampo, *Adv. Energy Mater.*, 2017, **7**, 1700264-n/a.

3 M. A. Green, E. D. Dunlop, J. Hohl-Ebinger, M. Yoshita, N. Kopidakis and A. W. Y. Ho-Baillie, *Prog. Photovolt. Res. Appl.*, 2020, **28**, 3–15.

4 National Renewable Energy Laboratory, NREL Best Research-Cell Efficiency Chart, https://www.nrel.gov/pv/assets/pdfs/best-research-cell-efficiencies.20200406.pdf, (accessed April 14, 2020).

5 P. Luo, S. Zhou, W. Xia, J. Cheng, C. Xu and Y. Lu, *Adv. Mater. Interfaces*, 2018, **4**, 1600970.

6 R. Swartwout, M. T. Hoerantner and V. Bulović, *ENERGY Environ. Mater.*, 2019, **2**, 119–145.

7 Y. Peng, G. Jing and T. Cui, *J. Mater. Chem. A*, 2015, **3**, 12436–12442.

8 M.-H. Li, H.-H. Yeh, Y.-H. Chiang, U.-S. Jeng, C.-J. Su, H.-W. Shiu, Y.-J. Hsu, N. Kosugi, T. Ohigashi, Y.-A. Chen, P.-S. Shen, P. Chen and T.-F. Guo, *Adv. Mater.*, 2018, **30**, 1801401.

9 P. Luo, Z. Liu, W. Xia, C. Yuan, J. Cheng and Y. Lu, *J. Mater. Chem. A*, 2015, **3**, 12443–12451.

10 X. Wei, Y. Peng, G. Jing and T. Cui, *Jpn. J. Appl. Phys.*, 2018, **57**, 052301.

11 J. Yin, H. Qu, J. Cao, H. Tai, J. Li and N. Zheng, *J. Mater. Chem. A*, 2016, **4**, 13203–13210.

12 Y. Jiang, M. R. Leyden, L. Qiu, S. Wang, L. K. Ono, Z. Wu, E. J. Juarez-Perez and Y. Qi, *Adv. Funct. Mater.*, 1703835-n/a.

13 G. Tong, H. Li, G. Li, T. Zhang, C. Li, L. Yu, J. Xu, Y. Jiang, Y. Shi and K. Chen, *Nano Energy*, 2018, **48**, 536–542.

14 L. Qiu, S. He, Y. Jiang, D.-Y. Son, L. K. Ono, Z. Liu, T. Kim, T. Bouloumis, S. Kazaoui and Y. Qi, *J. Mater. Chem. A*, 2019, **7**, 6920–6929.

15 C. Yi, J. Luo, S. Meloni, A. Boziki, N. Ashari-Astani, C. Grätzel, S. M. Zakeeruddin, U. Röthlisberger and M. Grätzel, *Energy Environ. Sci.*, 2016, **9**, 656–662.

16 G. Liu, H. Zheng, X. Xu, L.-Z. Zhu, X. Zhang and X. Pan, *Chem. Mater.*, 2018, **30**, 7691–7698.

17 M. Saliba, T. Matsui, J.-Y. Seo, K. Domanski, J.-P. Correa-Baena, M. Khaja Nazeeruddin, S. M. Zakeeruddin, W. Tress, A. Abate, A. Hagfeldt and M. Grätzel, *Energy Environ. Sci.*, 2016, **9**, 1989–1997.

18 A. Ummadisingu and M. Grätzel, *Sci. Adv.*, 2018, **4**, e1701402.

19 D. F. Swinehart, *J. Chem. Educ.*, 1962, **39**, 333.

20 M. R. Leyden, M. V. Lee, S. R. Raga and Y. Qi, *J. Mater. Chem. A*, 2015, **3**, 16097–16103.

21 M. T. Hoerantner, E. L. Wassweiler, H. Zhang, A. Panda, M. Nasilowski, A. Osherov, R. Swartwout, A. E. Driscoll, N. S. Moody, M. G. Bawendi, K. F. Jensen and V. Bulović, *ACS Appl. Mater. Interfaces*, 2019, **11**, 32928–32936.

22 V. S. Chirvony, K. S. Sekerbayev, D. Pérez-del-Rey, J. P. Martínez-Pastor, F. Palazon, P. P. Boix, T. I. Taurbayev, M. Sessolo and H. J. Bolink, *J. Phys. Chem. Lett.*, 2019, **10**, 5167–5172.

23 J. Li, H. Wang, X. Y. Chin, H. A. Dewi, K. Vergeer, T. W. Goh, J. W. M. Lim, J. H. Lew, K. P. Loh, C. Soci, T. C. Sum, H. J. Bolink, N. Mathews, S. Mhaisalkar and A. Bruno, *Joule*, , DOI:10.1016/j.joule.2020.03.005.

24 T. Kirchartz, J. A. Márquez, M. Stolterfoht and T. Unold, *Adv. Energy Mater.*, **n/a**, 1904134.

25 M. Stolterfoht, P. Caprioglio, C. M. Wolff, J. A. Márquez, J. Nordmann, S. Zhang, D. Rothhardt, U. Hörmann, A. Redinger, L. Kegelmann, S. Albrecht, T. Kirchartz, M. Saliba, T. Unold and D. Neher, *ArXiv181001333 Phys.*

26 F. Fu, T. Feurer, T. P. Weiss, S. Pisoni, E. Avancini, C. Andres, S. Buecheler and A. N. Tiwari, *Nat. Energy*, 2017, **2**, 16190.

27 Y. Jiang, T. Feurer, R. Carron, G. T. Sevilla, T. Moser, S. Pisoni, R. Erni, M. D. Rossell, M. Ochoa, R. Hertwig, A. N. Tiwari and F. Fu, *ACS Nano*, 2020, **14**, 7502–7512.

